Long-range FRET-mediated exciton diffusion in 2D assemblies of CsPbBr₃ perovskite nanocrystals

Erika Penzo,[1]* Anna Loiudice,[2] Edward S. Barnard,[1] Nicholas J. Borys,[1†] Matthew J. Jurow,[1,3]

Monica Lorenzon,[1] Igor Rajzbaum,[1] Edward K. Wong,[1] Yi Liu,[1,3] Adam M. Schwartzberg,[1]

Stefano Cabrini,[1] Stephen Whitelam,[1] Raffaella Buonsanti,[2] Alexander Weber-Bargioni[1]**

[1] Molecular Foundry, Lawrence Berkeley National Laboratory, Berkeley, CA 94720, USA

[2] Institute of Chemical Sciences and Engineering of the École Polytechnique Fédérale de Lausanne, Switzerland

[3] Materials Sciences Division, Lawrence Berkeley National Laboratory, Berkeley, CA 94720, USA

1

ABSTRACT

Förster Resonant Energy Transfer (FRET)-mediated exciton diffusion through artificial nanoscale building block assemblies could be used as a new optoelectronic design element to transport energy. However, so far nanocrystal (NC) systems supported only diffusion length of 30 nm, which are too small to be useful in devices. Here, we demonstrate a FRET-mediated exciton diffusion length of 200 nm with 0.5 cm^2/s diffusivity through an ordered, two-dimensional assembly of cesium lead bromide perovskite nanocrystals (PNC). Exciton diffusion was directly measured via steady-state and time-resolved photoluminescence (PL) microscopy, with physical modeling providing deeper insight into the transport process. This exceptionally efficient exciton transport is facilitated by PNCs' high PL quantum yield, large absorption cross-section, and high polarizability, together with minimal energetic and geometric disorder of the assembly. This FRET-mediated exciton diffusion length matches perovskites' optical absorption depth, opening the possibility to design new optoelectronic device architectures with improved performances, and providing insight into the high conversion efficiencies of PNC-based optoelectronic devices.

Manuscript

The mechanism of Förster Resonant Energy Transfer (FRET)-mediated exciton transport is poorly understood, specifically in terms of transport length, dynamics, and coherence. Better understanding of FRET would allow us to engineer artificial nanoscale building block assemblies with efficient, long-range exciton propagation and novel optoelectronic devices[1]: natural systems, such as photosystem II, display FRET-mediated energy transfer with μm diffusion lengths[2]. Excitonic transport a critical property of modern optoelectronic devices, such as flexible organic light-emitting diodes (OLEDs), solar cells, and light modulators;[3] it also enables rich quantum and nanoscale phenomena such as Bose-Einstein condensation[4] and exciton fission.[5] Artificial nanoscale building block assemblies are characterized by relatively short FRET-mediated exciton diffusion lengths, typically on the order of 10 nm in organic semiconductors[6] and 30 nm in inorganic nanocrystal (NC) solids,[7] which is a major limitation to the exploration of new exciton-based optoelectronic phenomena and to the development of new optoelectronic devices. Here we show that, within close-packed, two-dimensional assemblies of isoenergetic perovskite nanocrystals (PNCs), FRET-mediated exciton diffusion lengths reach 200 nm, close to the light absorption depth of 200-400 nm for this class of materials,[8-9] and the so far longest reported FRET-mediated exciton diffusion length in a NC system.

The Förster equation describes the structural and optoelectronic requirements between a donor-acceptor system to maximize the FRET rate: [10]

$$1/\tau_{DA} = \frac{2\pi}{\hbar} \frac{\mu_D^2 \mu_A^2 \kappa^2}{r_{DA}^6 n^4}$$

$1/\tau_{DA}$ is the hopping rate between Donor (D) particle and Acceptor (A) particle with τ_{DA} the average time for an exciton to hop from donor to acceptor. Maximizing this hopping rate requires (1) minimizing inter-particle distances r and the refractive index n, while (2) maximizing the spectral overlap between donors and acceptors $\mu_D^2\mu_A^2$, and (3) aligning the dipole moments to maximize the orientation factor κ^2. Additional parameters critical to experimentally study the transport are maximizing the polarizability of individual emitters to enhance (4) photon absorption and hence exciton creation, (5) the fluorescent quantum yield for an optimized signal-to-noise ratio, and (6) a flat energy landscape between the particles (small inhomogeneous line broadening). Importantly, these 6 parameters affect the exciton diffusion multiplicatively, meaning that if one parameter is poorly optimized, exciton diffusion can be completely suppressed. Hence, most studies of exciton transport through nanoscale building block assemblies find exciton diffusion length of 6-30 nm (diffusion coefficient of $0.2\text{-}12\times10^{-3}$ cm^2/s) for chalcogen-based quantum dot (QD) assemblies [7, 11-12], and of 3-50 nm for organic systems where the exciton transport occurs via singlet emitters and therefore FRET.[13-16] The short diffusion lengths are attributed to one or several of these parameters to be limiting, e.g. for QD assemblies excitonic traps and spatial disorder have been attributed to relatively short transport.

PNCs are a new fascinating NC class with the potential to excel in all of these parameters. As bulk semiconductors, lead halide perovskites have emerged as a promising new class of materials for low-cost, solution-processable optoelectronics,[17-20] demonstrating thin-film solar cell power conversion efficiencies exceeding 25%[21-22] and LEDs with 20% external quantum efficiency.[23-26] In the form of NCs, the all inorganic cesium lead halide (CsPbX$_3$, X = I, Br, or Cl) PNCs provide high optical tunability as a function of composition,[27-30] size, [29, 31-34] and shape, [31-32, 35] with impressive exciton generation efficiency, [36] and scalable solution-phase processes.[37-40] In terms of

FRET-mediated transport they optimize all 6 parameters: (1) The inter-particle distance r is determined by the ligand (oleic acid and oleylamine) and amounts to 2 nm. (2) The spectral overlap is high due to narrow emission linewidths[27] and small Stokes shifts.[27] Furthermore, their defect-tolerant optical emission (responsible for record efficiencies in QD solar cells[28]) maintains the symmetric and narrow emission bands compared to chalcogen based NCs, [20] and hence the high spectral overlap. The transition dipoles (3) between adjacent PNCs have been reported to be well-aligned as well,[41] due to their cubic shape directing the overall orientation in a self-assembled layer. PNCs have also demonstrated a combination of high photon absorption crosssection (4) and near unity quantum yield (5).[42] A flat energy landscape (6) among NCs to reduce excitonic traps can be obtained by controlling the NC size in a weakly quantum confined regime where the energy bandgap is primarily determined by the chemical composition.[27]

In this work we show that indeed, FRET-mediated exciton transport through self-assembled close-packed PNC mono layers reaches over 200 nm with a diffusivity of ~ 0.1 cm^2/s, which is in terms of diffusion length one order of magnitude higher and in terms of diffusivity two orders of magnitude larger than previously reported for chalcogen based QDs.[7] We demonstrated these values by studying the exciton diffusion in a close-packed monolayer of CsPbBr$_3$ PNCs that confines the available states for exciton propagation in 2D, allowing for the direct visualization of exciton diffusion by PL microscopy. The diffusion length and the diffusivity were determined via stead state PL microscopy mapping and the diffusivity using time resolved PL mapping, respectively. The diffusion was modeled using continuum and discrete representations of exciton hopping to provide a physical interpretation of our experiments, showing that albeit demonstrating record FRET mediated exciton diffusion length, our system is still in a sub-diffusive regime.

To simplify the direct visualization of exciton transport we confined the PNCs in a self-assembled monolayer on a Si wafer with about 1 nm of native oxide and coated with ~10 nm of polymer to prevent both exciton quenching into the Si and wave-guiding along the dielectric layer. We made two kinds of samples, a close-packed sample to study the exciton diffusion, and a control sample with a sparse layer of small groups of PNCs separated by at least 20 nm to prevent FRET based diffusion. The NCs examined in this study were cubic $CsPbBr_3$ PNCs with an average side length of 10 nm, synthesized according to an established procedure.[27] Spin-coating from a toluene solution on a surface functionalized with a –CH terminated polymer reproducibly yielded close-packed monolayers with an inter-particle spacing of ~2 nm, which is determined by the ligand length (see Fig. 1, Methods, and the SI for a detailed description of the sample preparation methods). In order to stabilize the PNCs during optical characterization (conducted at room temperature and under ambient atmosphere), we adapted a recently reported passivation process:[43] after spin-coating the solution of PNCs, we deposited ~3 nm of aluminum oxide by plasma-assisted atomic layer deposition (ALD). The passivated samples emitted stable PL upon illumination with continuous wave (CW) laser powers as high as 2000 W/cm^2 or with pulsed laser fluences as high as 50 $\mu J/cm^2$.
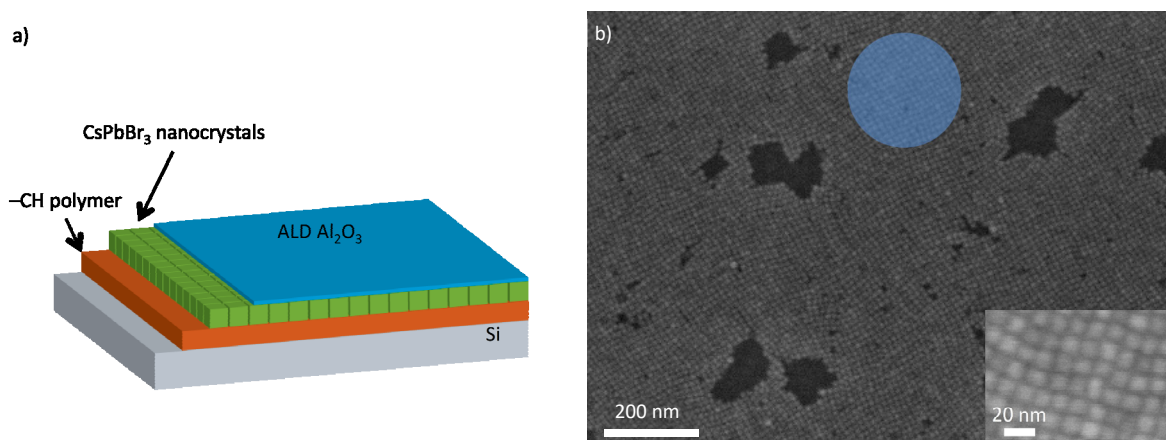
Figure 1. Deposition of controlled PNC 2D architectures. (a) CsPbBr3 PNCs in toluene were spin-coated onto a Si substrate functionalized with a –CH terminated polymer and coated with 3 nm of aluminum oxide deposited by ALD to prevent degradation during measurements. (b) SEM micrograph of a close-packed monolayer of PNCs. The blue circle shows the size (FWHM ~200nm) of the excitation laser spot used in subsequent optical experiments.

Exciton diffusion in NC solids and organic semiconductors has predominantly been studied indirectly by spectroscopic techniques, which can only provide a coarse estimate of the diffusion length.[12, 44] Recent microscopy-based approaches allow for the direct measurement of diffusion dynamics including the two main quantities that characterize exciton diffusion: the diffusion length and the diffusion coefficient (or diffusivity). [7]

Figure 2 illustrates the basic principles of the visualization of exciton diffusion. In order to measure the diffusion length and coefficient, we start by exposing the PNCs monolayer to a perpendicular laser beam, whose size is kept as close as possible to the diffraction limit. The laser beam generates a local population of excited states in the PNCs monolayer, with an initial spatial distribution that matches the intensity profile of the excitation spot. The PL maps were recorded with a CCD camera, after sample excitation with a 450nm laser, whose spot was kept as close as possible to the diffraction limit, with a FWHM of 240nm (Supplementary Fig. S18). If the motion

7

of an exciton is allowed, for instance by FRET-induced hopping onto a nearby PNC, then it is possible that such exciton will travel before radiatively recombining. Our sample preparation greatly enhances the probability of such hopping by promoting the self-assembly of the PNCs in a close-packed monolayer. Excitons can therefore propagate within the 2D plane of the monolayer, which ultimately results in a radial expansion from the excited state distribution (Figure 2a) and in a broader spot of the collected PL with respect to the excitation spot. Conversely, if the distance increases with respect to the close-packed case, the FRET-hopping is not allowed, and the emission can only occur from the same PNC that was initially excited (Figure2b). In order to better understand this effect, we report in Figure 2b-c two images of PNCs, one in a close-packed lattice and the other one when the PNCs are spincoated onto a non-engineered substrate, thus resulting in a random distribution where each PNCs is far enough from others (at least 20nm) to hinder FRET transport. The collected PL from such samples are reported in Figure 2e,f. Here, we can appreciate the significantly different results of the excitation with the same spot, shape and energy: the spatial extent of the PL map collected from the close-packed sample is much broader than the excitation spot, whereas in the sample in which excitons cannot hop the spatial extent of the PL map resembles the excitation spot, only slightly enlarged due to the convolution of the point-spread function of the microscope with the spatial profile of the excitation spot PNC (i.e., a convolution of a diffraction-limited point source with the diffraction-limited spot of a focused laser beam; see Supplementary Fig. S18). A schematic of the set-up is shown in Supplementary Fig. S19. In order to provide a more quantitative comparison between the two images, in Figure 2g we report a line scan through both PL maps as extracted from Figures 2e-f. Both spots are radially symmetric, so we can take any direction in each spot and compare their relative cross-section. Remarkably, in first order approximation it is possible to describe the diffusion profile within a Gaussian

framework. By subtracting the variances of the Gaussian fits with and without diffusion (close-packed vs sparse monolayer), we obtain a first estimate of the diffusion length, as explained in detail in the Supporting Information (see sections S2, S4, and S6 of the SI for details). For comparison, we also calculated a diffusion length by modeling the steady state diffusion using continuum equations and microscopic simulations (see SI sections S3 to S6). Modeling exciton creation, recombination, and hopping indicates that our PL profiles are consistent with a mean excitonic diffusion constant of the order of 0.5 cm^2/s, or $(224 \text{ nm})^2$/ns, which results in a characteristic exciton diffusion length of about 200 nm (consistent with the simple estimate in which we approximate profiles as Gaussian distributions). Using a model that assumes a completely uniform film of NCs, subtle but significant variations occur between the tails of measured and predicted profiles. However, as seen in the SEM, vacancies occur in the experimental film (Fig. 1b). These vacancies can inhibit further exciton propagation, and when they are included in the model the predicted PL profiles reproduces the experimental PL profile more closely (Fig. 2g).

Importantly, the excitation power in all measurements was kept sufficiently low so as to remain in the linear excitation regime (see Methods and Supplementary Fig. S23). The presented interpretation of deconvolving the Gaussian distributions and extracting the diffusion lengths is only correct in the regime where PL intensity scales linearly with the excitation power. At higher pump fluences, exciton-exciton annihilation starts taking place, thus introducing an additional term in the diffusion equations that may lead to significantly broader PL profiles that could be interpreted as enhanced exciton diffusion, while actually it is related to a steep exciton concentration gradient and the effective diffusion length for each exciton is still the same. A detailed discussion is reported in the Supporting Information.
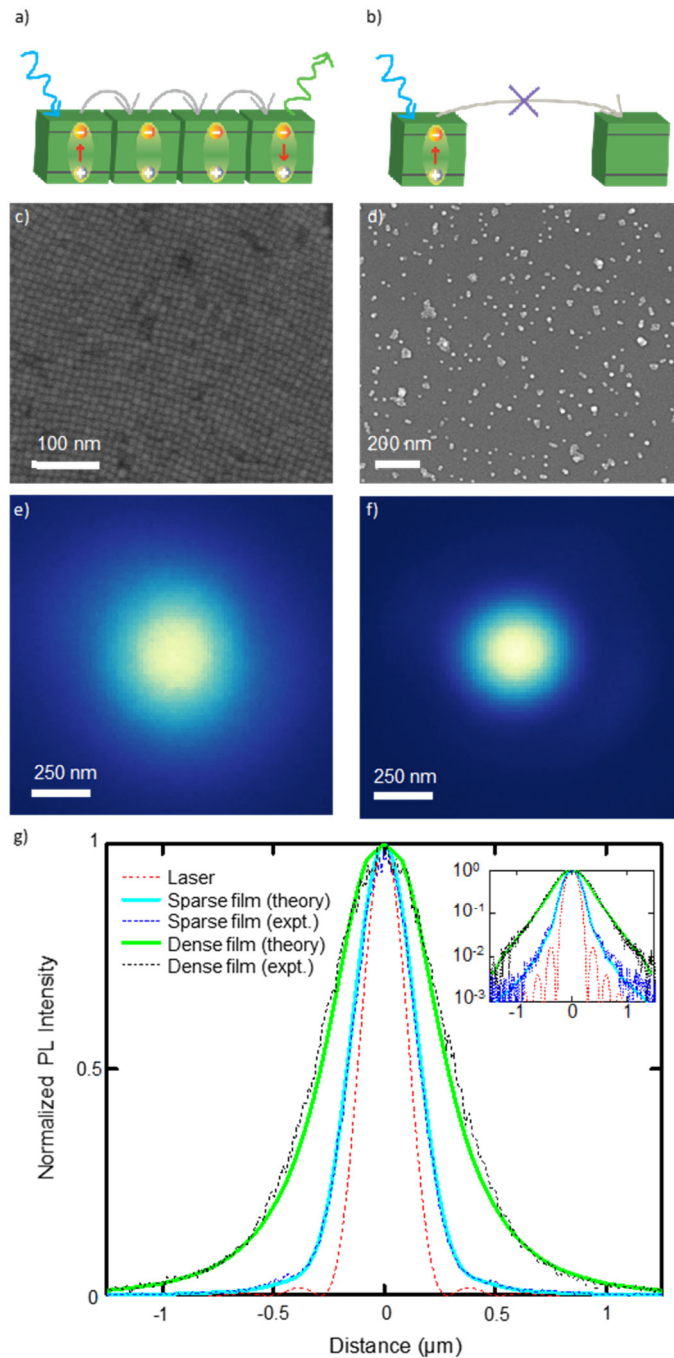
Figure 2. Direct measurement of steady-state exciton diffusion. (a) When PNCs are assembled in a close-packed monolayer, the distance between NCs is minimized, allowing for efficient FRET-mediated exciton diffusion. (b) When PNCs are spatially separated, FRET-mediated exciton diffusion is inhibited. (c) SEM micrograph of a close-packed monolayer of PNCs. (d) SEM

micrograph of a sparse monolayer of PNCs. (e) Normalized PL intensity profile emitted by the close-packed PNCs monolayer when excited with a diffraction-limited laser spot with wavelength 450 nm. (f) Normalized PL intensity profile emitted by the sparse PNCs monolayer when excited with a diffraction-limited laser spot with wavelength 450 nm. (g) PL profile cross-sections of panel (e) (black dashed line) and (f) (blue dashed line) together with simulated PL profile cross-sections for a square lattice of nanoparticles with a vacancy fraction of 20% (green line), and for a sparse sample of nanoparticles on which hopping cannot occur (cyan line). The dashed red line corresponds to the excitation laser profile cross-section. The inset shows the main figure on a logarithmic vertical scale.

CsPbBr$_3$ PNCs are not strongly quantum confined in the size range used in this study (10 nm average cube side);[27] as a result, our close-packed monolayers mostly constitute a flat energy landscape for exciton diffusion, which is a requirement to maximize FRET in a NC solid. In the presence of energetic heterogeneity, excitons travel downhill in energy and get trapped in NCs with smaller bandgaps (once excitons relax to lower energies they cannot diffuse to NCs with larger bandgaps). In this system, because excitations are more efficiently funneled from high-energy to low-energy states than vice-versa, signatures of this inhomogeneity-driven process can be discerned in the temporal evolution of the PL spectrum after pulsed excitation. The additional energy transfer relaxation channels of the high-energy sites accelerate their relaxation rates, yielding energy-dependent excited-state lifetimes, where higher-energy NCs have shorter lifetimes than those with lower-energies. Thus, following pulsed excitation, the PL spectrum typically shifts to lower energies as the higher-energy NCs relax more rapidly than the low-energy NCs. Experimentally, this behavior can be resolved as time-dependent shifts in the PL spectrum to lower energy or emission energy-dependent relaxation kinetics. In colloidal semiconducting NCs, this

energetic heterogeneity largely arises from the polydispersity of the sample where the larger quantum dots are less quantum confined, have lower-energy excited states, and thus serve as exciton traps when arranged into a quasi-continuous film.[45-46]

In Figure 3, we used time-resolved PL (TRPL) spectroscopy to assess the disorder in the energetic landscape in our films. As shown in Fig. 3a, during the assembly process, energy minimization pushes the PNCs of different size to the edges of the ordered, close-packed regions. The result is that the central regions of the film are significantly less polydisperse than the edges. Examples of a uniform area (top dashed rectangle) and of a non-uniform area (bottom dashed rectangle) are highlighted in Fig. 3a. As seen in Figs. 1b and 2c, the exciton diffusion studies were performed in the regions with monodisperse PNCs; in these portions of the film time-resolved PL spectroscopy measurements displayed identical decay kinetics for the high and low energy components of the PL spectrum (Fig. 3b) and, accordingly, the PL spectrum does not change with time (Supplementary Fig. S20). In contrast, in the edge regions with maximal polydispersity, signatures of excitons getting trapped in lower-energy bandgap NCs were subtle but detectable: the lower energy emission (2 nm band; centered at 529.2 nm) decays slower than the higher-energy emission (2 nm band; centered at 502.6 nm) and the PL spectrum exhibits a clear evolution to lower energies following pulsed excitation (Supplementary Fig. S20). These results indicate that within the central regions of the film, the site-to-site variations in energy are minimized thus, strongly reducing, or possibly eliminating, exciton trapping due to low-energy sites. Therefore, only at the edges, where the polydispersity is maximal, we see evidence of an energetic landscape that is littered with traps for the excitons. Rather, in the central regions, the weak quantum confinement combined with the assembly process play a pivotal role in achieving the long exciton diffusion distance.
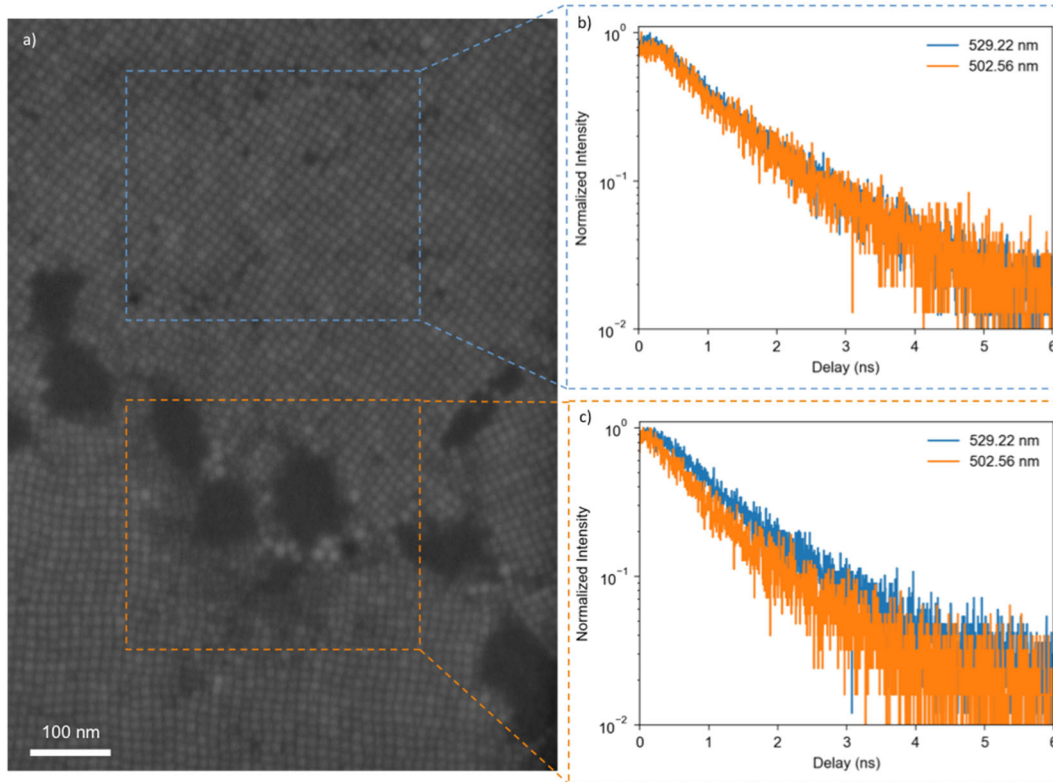
Figure 3. Probing the energy landscape by time-resolved PL spectroscopy. (a) SEM micrograph of a close-packed monolayer of PNCs showing ordered areas made of uniformly sized PNCs (blue dashed rectangle) and disordered areas made of PNCs of different sizes at a crack in the film (orange dashed rectangle). (b) PL intensity as a function of time at two emission wavelengths, 529.22 nm (blue) and 500.56 nm (orange), measured on an ordered area made of uniformly sized PNCs. The overlap of the curves indicates equivalent PL lifetimes at both emission wavelengths. (c) PL intensity as a function of time at two emission wavelengths, 529.22 nm (blue) and 500.56 nm (orange), measured on a disordered area made of PNCs of different sizes. The orange curve displays the slower decay of the low energy portion of the PL spectrum, due to exciton migration to smaller bandgap PNCs.

To better understand and measure the dynamics of the long-distance exciton diffusion, time-resolved PL microscopy was employed to track the temporal evolution of the PL spatial profile as it expanded from its initial state. Areas of the close-packed monolayer of monodisperse PNCs were excited with short laser pulses and the magnified PL emission (100×) was collected by a single mode fiber (with a diameter of 5 μm). To gain spatial resolution, the collection fiber was mounted on a translation stage that systematically scanned the fiber aperture in the focal plane of the microscope. At each fiber position, a full time-resolved PL transient was recorded, which allowed us to track how the excited state expanded with time. The temporal evolution of the normalized PL profile is shown in Figure 4a, where the 0 nm distance corresponds to the position of the fiber, which is aligned with the center of the PL spot. Distances greater than zero are reported as the distance between the center of the PL spot and the center of the image of the fiber aperture on the sample plane. The spatially and time-resolved PL trace in Figure 4a clearly displays the expected diffusive broadening, which can be quantified by calculating the PL profile width at each time slice (Fig. 4b). The rate at which the variance of the spatial PL profile (Gaussian fit) rises with time is sub-linear, indicating a sub-diffusive process, which, as discussed above, is very likely due to PNC voids in the film. In these dynamic measurements, as reported in previous work,[7] the average exciton diffusion length is calculated as the increase in the PL profile variance from its initial state (right after excitation) to the average lifetime of the system. The average lifetime of these PNCs in a close-packed film is 1.14 ns (as calculated as the time to reach a decay of 37% or 1/e of the PL intensity, see Supplementary Fig. S21), which, using the dynamics in Figure 4b, yields an average exciton diffusion length of 194 nm that is in very good agreement with that derived from our steady-state measurements.

The PL lifetime was also calculated at each point (a PL lifetime map is shown in Supplementary Fig. S22) and was observed to decrease as the reciprocal of the PL intensity (Fig. 4c). This spatially dependent change in dynamics is an expected effect of the diffusion process, which is driven by the exciton density gradient, and results in a larger net outward exciton flux in areas with a large exciton population. The minimum lifetime was found to be 1 ns, and grew to 1.3 ns 500 nm away from the excitation intensity maximum. Note that because the measurements were performed with excitation intensities that are deep in the linear regime of the power-dependence of the PL (see Supplementary Fig. S23), we exclude the possibility that the central decrease in lifetime is due to higher order non-radiative recombination processes (e.g. Auger recombination).

The diffusion coefficient (or diffusivity) was calculated as the first derivative of the PL profile variance increase in time and is shown in Figure 4d. The effective diffusivity was found to decrease with time, from 0.5 cm^2/s right after excitation to ~ 0.1 cm^2/s at the end of the diffusion process.

These values of FRET-mediated exciton diffusion length and diffusivity are the largest reported so far for NC solids. Chalcogen-based QDs demonstrated diffusion lengths in the range of 20-30 nm and diffusivities between 0.2E-3 cm^2/s and 1.5E-3 cm^2/s.[7] The system here reported demonstrated one order of magnitude higher diffusion length and about two orders of magnitude higher diffusivity. Significantly, the exciton diffusion dynamics in our PNC films is comparable with that of unbound charge carriers in other bulk perovskite materials. Individual crystals of $CsPbI_2Br$ perovskite measured by pump-probe microscopy revealed a diffusivity of 0.27 cm^2/s,[47] and thin films of polycrystalline hybrid perovskite measured by transient absorption microscopy showed a diffusivity in the range of 0.05 cm^2/s to 0.08 cm^2/s, with diffusion lengths of 220 nm in the 2 ns experiment time.[48]
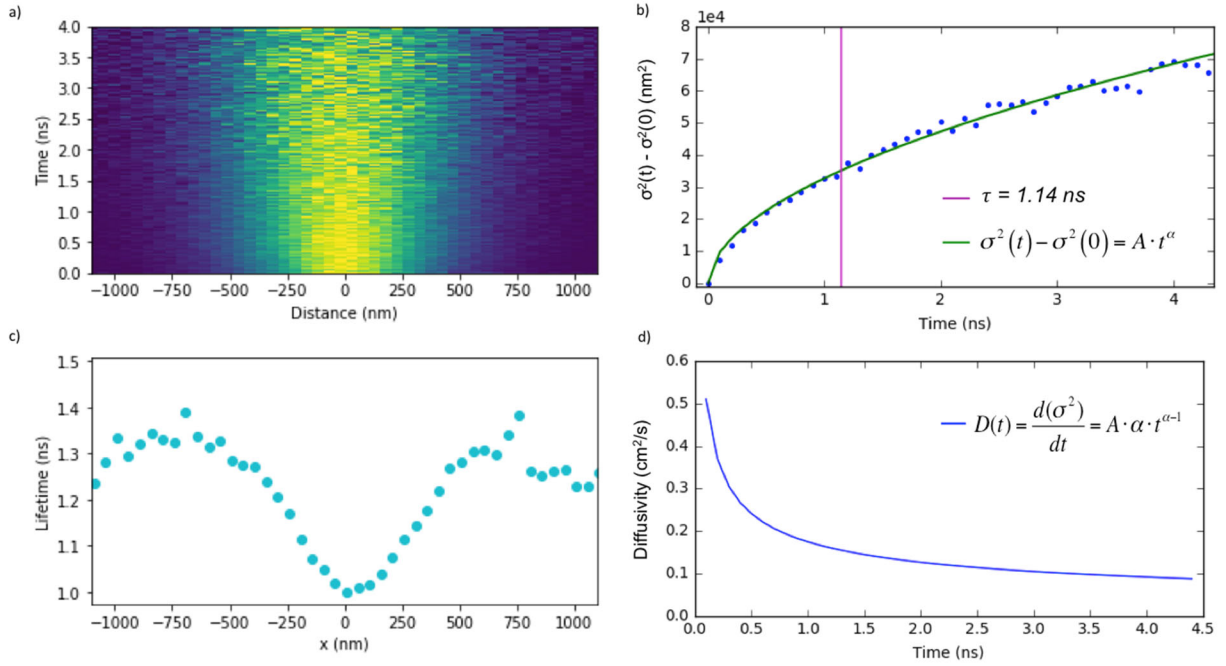
Figure 4. Probing exciton diffusion dynamics by time-resolved optical microscopy. (a) Time evolution of cross-sectional PL intensity profile. (b) PL profile variance increase as a function of time (blue dots). The green solid line shows the fit to the power law $A \cdot t^\alpha$ ($A = 0.3527$ cm^2/s , $\alpha = 0.53$). (c) Space-resolved PL lifetime calculated from the signal in (a) as the time for 37% or *1/e* decay of PL intensity. (d) Diffusivity (or diffusion coefficient) as a function of time calculated as the first derivative of the PL profile variance variation in (c).

In conclusion, ordered monolayers of isoenergetic PNCs were fabricated via controlled self-assembly. This system demonstrated extremely efficient FRET-mediated exciton diffusion, which was directly characterized by steady-state and time-resolved PL microscopy together with an analytical and statistical model that granted a deeper understanding of the exciton diffusion dynamics. Our measurements directly capture a diffusion length of 200 nm and a diffusivity of 0.5 cm^2/s. This diffusion length is ten times longer and the diffusivity is two orders of magnitude larger than previously reported values for films of chalcogen-based QDs,[7, 49] and comparable to

16

that of charge-carrier diffusion in thin films of polycrystalline hybrid perovskite.[48] Demonstrating such long-range diffusion, our PNC system is ideally suited to study FRET processes and FRET-mediated energy transfer on length scales that are easily accessible and therefore easy to optimize. Moreover, long exciton diffusion establishes an additional design element for next generation PNC-based optoelectronic devices.[20, 50]

Further progress towards even longer-range exciton diffusion may be achieved by improving PNCs energetic uniformity as well as by optimizing the protective ALD-based process that prevents perovskite degradation. Additionally, fabricating PNC assemblies with increased complexity, for example deliberately varying inter-particle distance in certain assembly portions or by positioning PNCs with decreasing bandgap next to each other forming an oriented energy funnel, could demonstrate ways to move excitons to predetermined positions. Overall, we showed that ordered assemblies of isoenergetic PNCs support FRET-mediated exciton diffusion at so far unprecedented lengths opening new possibilities for developing new optoelectronic devices.

METHODS

PNCs synthesis and characterization

CsPbBr$_3$ nanocubes were synthesized by a procedure adapted from the original report.[27] All chemicals were purchased from Sigma-Aldrich and used as received without further purification. Cs$_2$CO$_3$ (1.2 mmol) was added to 10 mL 1-octadecene and stirred at 120 °C under vacuum for 1 hour. Oleic Acid (2 mmol) was injected under nitrogen atmosphere and resulting mixture was stirred at 120 °C for two hours until fully dissolved. In a separate container, PbBr$_2$ (0.19 mmol) was added to 5 mL 1-octadecene and stirred at 120 °C under vacuum for 1 hour. Oleic acid (1.6 mmol) and oleylamine (1.5 mmol) were injected under nitrogen atmosphere. The resulting mixture was stirred at 120 °C for two hours until fully dissolved, then was heated to 165 °C. To this preheated lead solution was added 0.4 mL of hot Cs$_2$CO$_3$ solution under nitrogen atmosphere with vigorous stirring. Reaction was stirred for 5 seconds and cooled rapidly in ice bath until reaction mixture solidified. After freezing, reaction mixture was warmed to room temperature and transferred into centrifuge tubes. The mixture was centrifuged at 8,500 rpm, for 10 minutes. The supernatant was discarded, and the pellet was redispersed in anhydrous hexane (6 mL). An equal volume of tert-butanol was added to precipitate the NCs, and the mixture was centrifuged at 12,000 rpm for 15 minutes. The supernatant was discarded, and the pellet was redispersed in toluene. These solutions were then centrifuged for 5 minutes at 700 rpm, and the pellet was discarded to remove large aggregates. The supernatant was transferred to a glove box for film deposition.

PNCs monolayer fabrication

PNCs monolayers were prepared by spin coating (1,500 rpm, 45 s) from a colloidal suspension of nanocubes in toluene onto Si wafers coated with 10 nm of a –CH terminated polymer, which is sufficiently thin to prevent lateral wave-guiding but thick enough to prevent exciton quenching by the silicon. The concentration was 3 g/l for the close-packed monolayer and 60 mg/l for the sparse monolayer. The hydrocarbon polymer was deposited by polymerizing methane in a plasma

chamber (40 mTorr, RF power 100 W, 10 °C, Oxford Instruments). Aluminum oxide (3 nm) was deposited by plasma assisted atomic layer deposition at 40 °C (Oxford Instruments). Films were characterized by SEM (Zeiss).

Steady-state PL microscopy

The setup for steady-state PL microscopy is shown in Supplementary Figure S3a. The 450 nm CW diode laser source was collimated and then focused to a diffraction-limited spot by a 100X 0.95 NA objective lens. The back aperture of the objective was overfilled to assure diffraction-limited performance. Emission from the sample was collected by the same objective and additionally magnified 5.3X for a total magnification of 530X and imaged on a CCD camera (QSI SI 660 6.1mp Cooled CCD Camera) with pixel size 4.54 µm, which provided an effective imaging pixel size of 8.63 nm. A 490 nm long-pass dichroic filter (Semrock Di03-R488-t1) and two 496 nm long-pass edge filters (Semrock) were used to remove the excitation laser beam from the PL signal. The laser beam was imaged through the 490 nm long-pass dichroic filter (Semrock) and a 498 nm short-pass edge filter (Semrock) to remove the PL signal. Measurements were performed at 45 W/cm^2, which corresponds to the probability of one absorbed photon per 1,705 nanocubes during the 1.15 ns average lifetime.

Time-resolved PL spectroscopy

The setup for time-resolved PL microscopy is shown in Supplementary Figure S3b. The pulsed laser source (center wavelength 465 nm with a 2.5 nm bandwidth; 5 ps pulse duration; 40 MHz repetition rate) was collimated and focused by a 100X 0.95 NA objective lens. The back aperture of the objective was overfilled to assure diffraction-limited performance. Emission from the sample was collected by the same objective. A 490 nm long-pass dichroic filter (Semrock) and a

496 nm long-pass edge filter (Semrock) were used to remove the excitation laser beam from the PL signal. The PL spectral components were separated with a monochromator (Princeton Instruments Acton 2300i) and detected by a single-photon counting avalanche photodiode (MPD PDM series) connected to a time-correlated single-photon counting unit (Picoharp 300). The temporal resolution was approximately 50 ps as determined by the FWHM of the instrument response function.

Measurements were performed at laser fluence 2.5 μJ/ cm^2, which corresponds to the average probability of one absorbed photon per 32 nanocubes per pulse.

Time-resolved PL microscopy

The setup for time-resolved PL microscopy is shown in Supplementary Figure S3c. The pulsed laser source (center wavelength 465 nm with a 2.5 nm bandwidth; 5 ps pulse duration; 40 MHz repetition rate) was collimated and focused by a 100X 0.95 NA objective lens. The back aperture of the objective was overfilled to assure diffraction-limited performance. Emission from the sample was collected by the same objective and imaged on a single-mode fiber (P1-405P-FC-2, Thorlabs) attached to a translation stage (Attocube ECS series) that scanned the emission focal plane. The fiber mode field diameter was 2.5 – 3.4 μm at 480 nm; the stage was moved in 5 μm steps corresponding to 50 nm at the sample. A 490 nm long-pass dichroic filter (Semrock) and two 496 nm long-pass edge filters (Semrock) were used to remove the excitation laser beam from the PL signal. The laser beam was imaged through the 490 nm long-pass dichroic filter (Semrock) and a 498 nm short-pass edge filter (Semrock) to remove the PL signal. The signal was detected by a single-photon counting avalanche photodiode (MPD PDM-series) connected to a time-correlated

single-photon counting unit (Picoharp 300). The temporal resolution was approximately 50 ps, as determined by the FWHM of the instrument response function.

Measurements were performed at laser fluence 5 µJ/ cm^2, which corresponds to the average probability of one absorbed photon per 16 nanocubes per pulse.

The sample was mounted above the objective lens on a piezoelectric scanning stage. Samples were scanned during the course of the measurements (~30 min) over an area of 5×5 µm to avoid photobleaching or photodamage.

Physical modeling

We simulated the processes of exciton creation, recombination, and hopping at continuum- and microscopic levels of resolution. We convolved the resulting excitonic profiles with the optical point-spread function in order to calculate observed PL profiles. Full details of these calculations are given in SI sections S3 to S6.
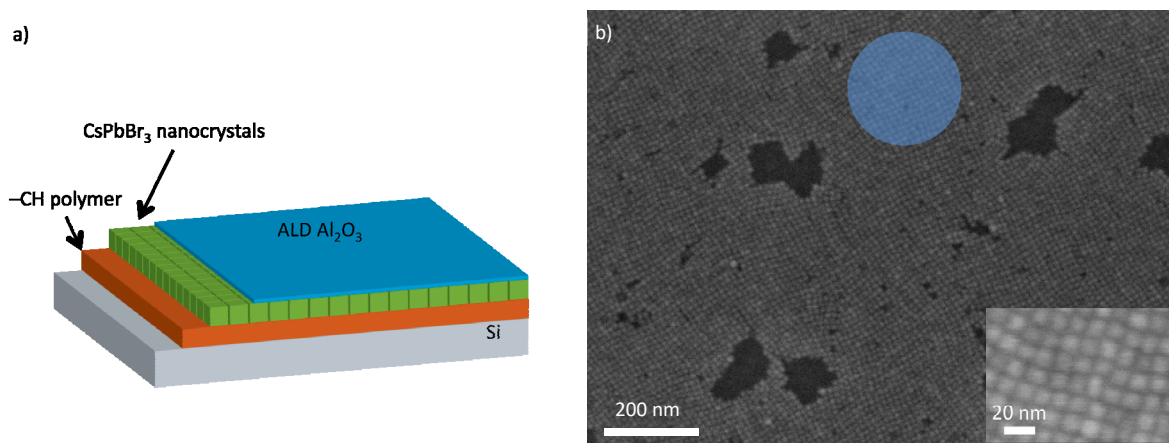
Fig. 1. Deposition of controlled PNC 2D architecture. (a) CsPbBr$_3$ PNCs in toluene were spin-coated onto a Si substrate functionalized with a –CH terminated polymer and coated with 3 nm of aluminum oxide deposited by ALD to prevent degradation during measurements. (b) SEM micrograph of a close-packed monolayer of PNCs. The blue circle shows the size (FWHM ~200nm) of the excitation laser spot used in subsequent optical experiments.
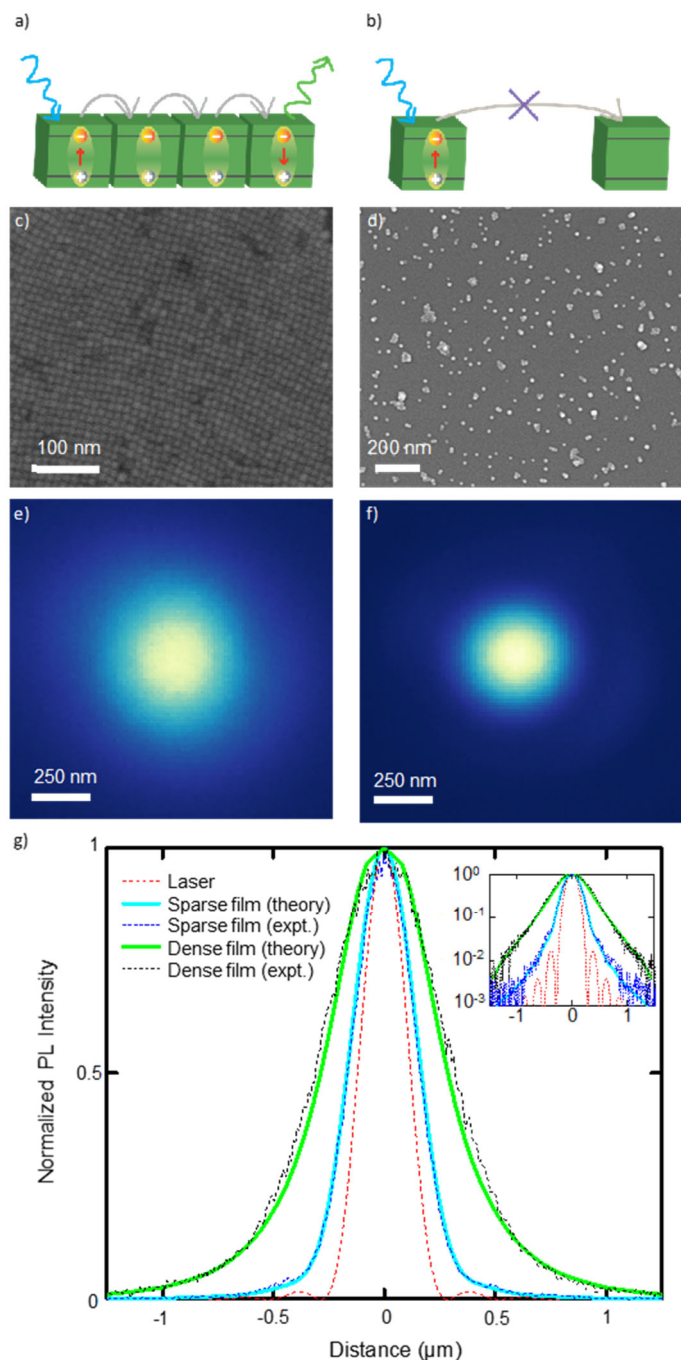
Figure 2. Direct measurement of steady-state exciton diffusion. (a) When PNCs are assembled in a close-packed monolayer, the distance between NCs is minimized, allowing for efficient FRET-mediated exciton diffusion. (b) When PNCs are spatially separated, FRET-mediated exciton diffusion is inhibited. (c) SEM micrograph of a close-packed monolayer of PNCs. (d) SEM

micrograph of a sparse monolayer of PNCs. (e) Normalized PL intensity profile emitted by the close-packed PNCs monolayer when excited with a diffraction-limited laser spot with wavelength 450 nm. (d) Normalized PL intensity profile emitted by the sparse PNCs monolayer when excited with a diffraction-limited laser spot with wavelength 450 nm. (g) PL profile cross-sections of panel (e) (black dashed line) and (f) (blue dashed line) together with simulated PL profile cross-sections for a square lattice of nanoparticles with a vacancy fraction of 20% (green line), and for a sparse sample of nanoparticles on which hopping cannot occur (cyan line). The dashed red line corresponds to the excitation laser profile cross-section. The inset shows the main figure on a logarithmic vertical scale.
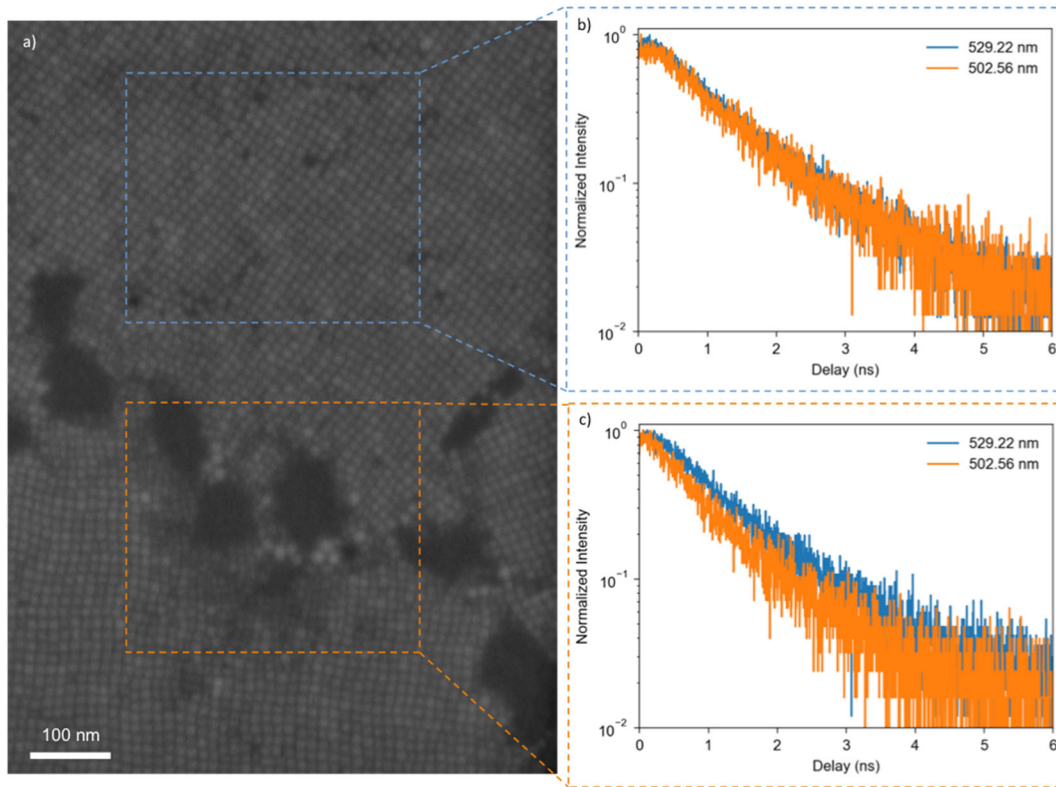
Figure 3. Probing the energy landscape by time-resolved PL spectroscopy. (a) SEM micrograph of a close-packed monolayer of PNCs showing ordered areas made of uniformly sized PNCs (blue dashed rectangle) and disordered areas made of PNCs of different sizes at a crack in the film (orange dashed rectangle). (b) PL intensity as a function of time at two emission wavelengths, 529.22 nm (blue) and 500.56 nm (orange), measured on an ordered area made of uniformly sized PNCs. The overlap of the curves indicates equivalent PL lifetimes at both emission wavelengths. (c) PL intensity as a function of time at two emission wavelengths, 529.22 nm (blue) and 500.56 nm (orange), measured on a disordered area made of PNCs of different sizes. The orange curve displays the slower decay of the low energy portion of the PL spectrum, due to exciton migration to smaller bandgap PNCs.
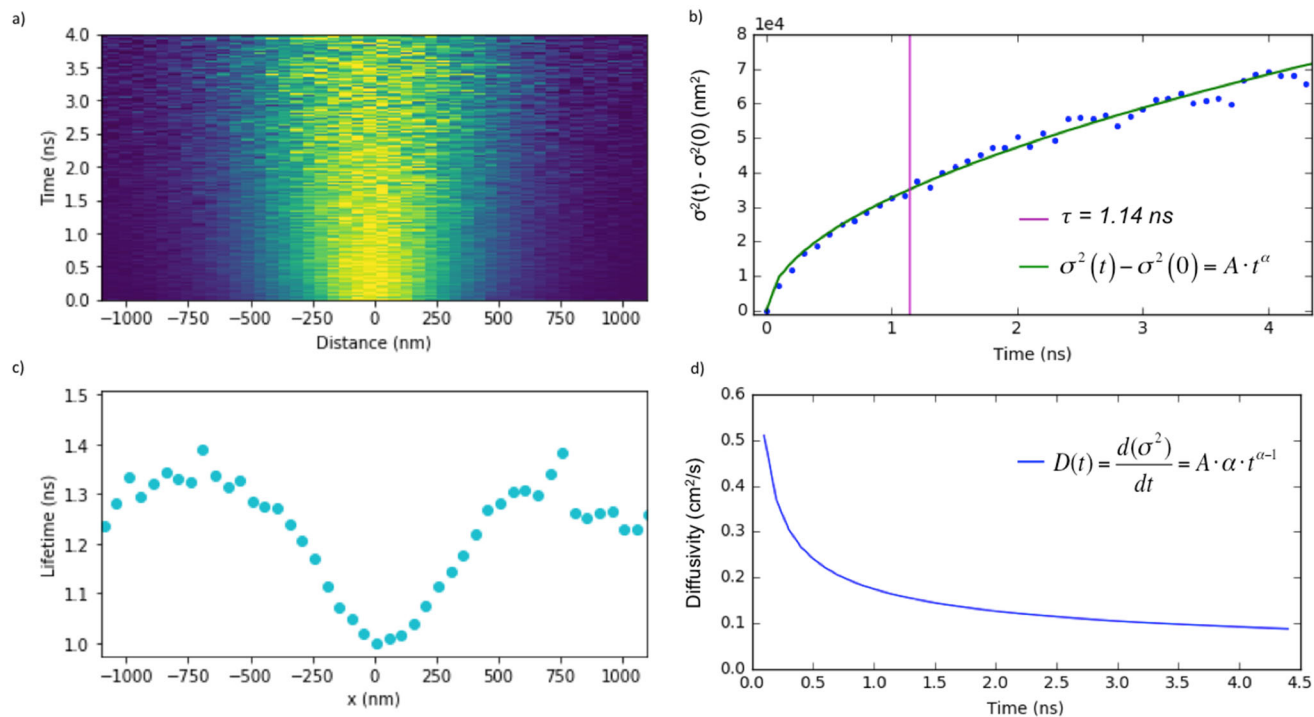
Figure 4. Probing exciton diffusion dynamics by time-resolved optical microscopy. (a) Time evolution of cross-sectional PL intensity profile. (b) PL profile variance increase as a function of time (blue dots). The green solid line shows the fit to the power law $A \cdot t^{\alpha}$ (A = 0.3527 cm^2/s , α = 0.53). (c) Space-resolved PL lifetime calculated from the signal in (a) as the time for 37% or *1/e* decay of PL intensity. (d) Diffusivity (or diffusion coefficient) as a function of time calculated as the first derivative of the PL profile variance variation in (c).

For Table of Contents Only

substrate
engineering

100 nm

500 nm

100 nm

500 nm

FRET-enabled
exciton
diffusion
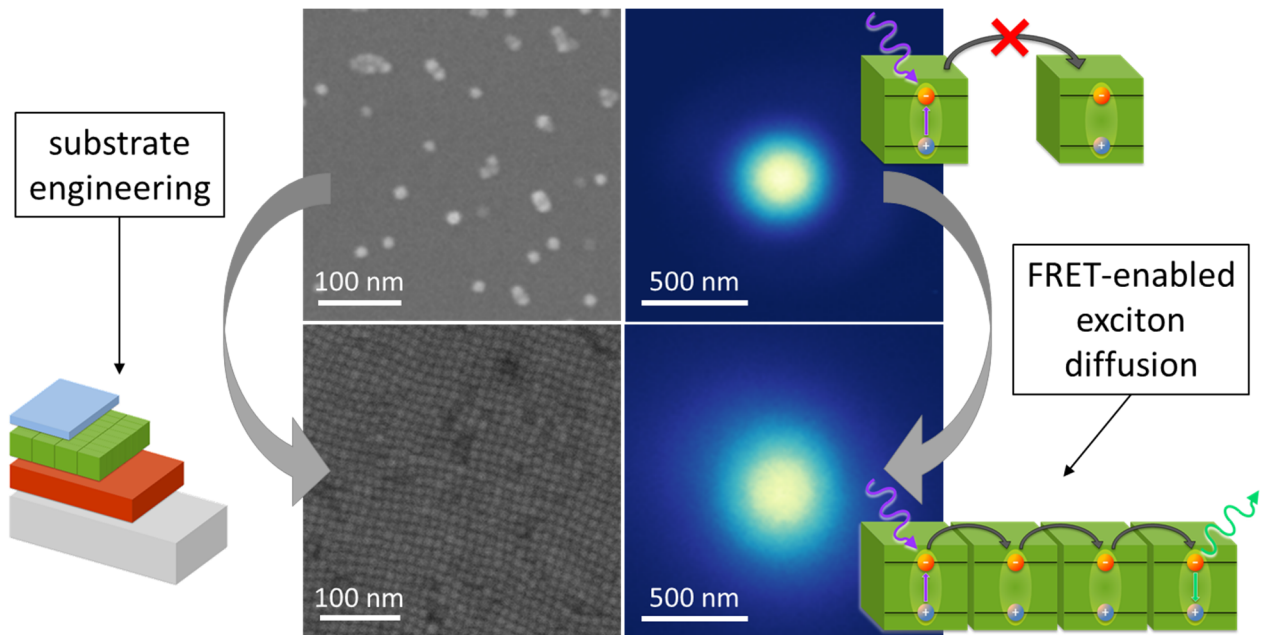
ASSOCIATED CONTENT

Supporting Information.

The following files are available free of charge.

Materials and methods, details of PNC monolayer fabrication, theoretical modeling, and additional figures. (PDF)

AUTHOR INFORMATION

Corresponding Author

* Erika Penzo erikapenzo@gmail.com *Alexander Weber-Bargioni awb@lbl.gov

Present Addresses

† Department of Physics, Montana State University, PO Box 173840, Bozeman, MT, 59717

Author Contributions

The manuscript was written through contributions of all authors. R.B. and A.W.-B. conceived the initial work. A.L. and I.R. performed initial experiments. E.P. prepared the samples, conducted the diffusion experiments and analysis, and wrote the manuscript. S.W. developed theoretical modeling and analysis. A.L. and M.J.J. synthesized the nanocrystals with supervision of R.B. and Y.L. E.S.B. and N.J.B. supported the experimental measurements and data analysis. E.P., E.K.W., and E.S.B. built the microscope. A.M.S. and S.C. supported the sample preparation and provided input into the data interpretation. E.P., E.S.B., N.J.B., M.J.J., A.M.S., S.W., M. L. and A.W.-B. helped with writing the manuscript. All authors have given approval to the final version of the manuscript.

REFERENCES

1.   Beljonne, D.; Curutchet, C.; Scholes, G. D.; Silbey, R. J., Beyond Forster Resonance Energy Transfer in Biological and Nanoscale Systems. *J Phys Chem B* **2009,** *113* (19), 6583-6599.
2.   Scholes, G. D.; Fleming, G. R.; Olaya-Castro, A.; van Grondelle, R., Lessons from nature about solar light harvesting. *Nat Chem* **2011,** *3* (10), 763-774.
3.   Lee, J.; Bao, W.; Ju, L.; Schuck, P. J.; Wang, F.; Weber-Bargioni, A., Switching Individual Quantum Dot Emission through Electrically Controlling Resonant Energy Transfer to Graphene. *Nano Lett* **2014,** *14* (12), 7115-7119.
4.   Plumhof, J. D.; Stoferle, T.; Mai, L. J.; Scherf, U.; Mahrt, R. F., Room-temperature Bose-Einstein condensation of cavity exciton-polaritons in a polymer. *Nat Mater* **2014,** *13* (3), 248-253.
5.   Congreve, D. N.; Lee, J. Y.; Thompson, N. J.; Hontz, E.; Yost, S. R.; Reusswig, P. D.; Bahlke, M. E.; Reineke, S.; Van Voorhis, T.; Baldo, M. A., External Quantum Efficiency Above 100% in a Singlet-Exciton-Fission-Based Organic Photovoltaic Cell. *Science* **2013,** *340* (6130), 334-337.
6.   Shaw, P. E.; Ruseckas, A.; Samuel, I. D. W., Exciton diffusion measurements in poly(3-hexylthiophene). *Adv Mater* **2008,** *20* (18), 3516-+.
7.   Akselrod, G. M.; Prins, F.; Poulikakos, L. V.; Lee, E. M. Y.; Weidman, M. C.; Mork, A. J.; Willard, A. P.; Bulovic, V.; Tisdale, W. A., Subdiffusive Exciton Transport in Quantum Dot Solids. *Nano Lett* **2014,** *14* (6), 3556-3562.
8.   Stranks, S. D.; Snaith, H. J., Metal-halide perovskites for photovoltaic and light-emitting devices. *Nat Nanotechnol* **2015,** *10* (5), 391-402.

9.   Stranks, S. D.; Eperon, G. E.; Grancini, G.; Menelaou, C.; Alcocer, M. J. P.; Leijtens, T.; Herz, L. M.; Petrozza, A.; Snaith, H. J., Electron-Hole Diffusion Lengths Exceeding 1 Micrometer in an Organometal Trihalide Perovskite Absorber. *Science* **2013,** *342* (6156), 341-344.

10.   Curutchet, C.; Franceschetti, A.; Zunger, A.; Scholes, G. D., Examining Forster energy transfer for semiconductor nanocrystalline quantum dot donors and acceptors. *J Phys Chem C* **2008,** *112* (35), 13336-13341.

11.   Kholmicheva, N.; Moroz, P.; Bastola, E.; Razgoniaeva, N.; Bocanegra, J.; Shaughnessy, M.; Porach, Z.; Khon, D.; Zamkov, M., Mapping the Exciton Diffusion in Semiconductor Nanocrystal Solids. *ACS Nano* **2015**.

12.   Kholmicheva, N.; Moroz, P.; Eckard, H.; Jensen, G.; Zamkov, M., Energy Transfer in Quantum Dot Solids. *Acs Energy Letters* **2017,** *2* (1), 154-160.

13.   Mikhnenko, O. V.; Blom, P. W. M.; Nguyen, T.-Q., Exciton diffusion in organic semiconductors. *Energy & Environmental Science* **2015,** *8* (7), 1867-1888.

14.   Lunt, R. R.; Giebink, N. C.; Belak, A. A.; Benziger, J. B.; Forrest, S. R., Exciton diffusion lengths of organic semiconductor thin films measured by spectrally resolved photoluminescence quenching. *Journal of Applied Physics* **2009,** *105* (5), 053711.

15.   Peumans, P.; Yakimov, A.; Forrest, S. R., Small molecular weight organic thin-film photodetectors and solar cells. *Journal of Applied Physics* **2003,** *93* (7), 3693-3723.

16.   Yang, L.-G.; Chen, H.-Z.; Wang, M., Optimal film thickness for exciton diffusion length measurement by photocurrent response in organic heterostructures. *Thin Solid Films* **2008,** *516* (21), 7701-7707.

17.   Brenner, T. M.; Egger, D. A.; Kronik, L.; Hodes, G.; Cahen, D., Hybrid organic-inorganic perovskites: low-cost semiconductors with intriguing charge-transport properties. *Nat Rev Mater* **2016,** *1* (1).

18.   Zhou, Y. Y.; Zhu, K., Perovskite Solar Cells Shine in the "Valley of the Sun". *Acs Energy Lett* **2016,** *1* (1), 64-67.

19.   Sutherland, B. R.; Sargent, E. H., Perovskite photonic sources. *Nat Photonics* **2016,** *10* (5), 295-302.

20.   Kovalenko, M. V.; Protesescu, L.; Bodnarchuk, M. I., Properties and potential optoelectronic applications of lead halide perovskite nanocrystals. *Science* **2017,** *358* (6364), 745-750.

21.   Zheng, X.; Hou, Y.; Bao, C.; Yin, J.; Yuan, F.; Huang, Z.; Song, K.; Liu, J.; Troughton, J.; Gasparini, N.; Zhou, C.; Lin, Y.; Xue, D.-J.; Chen, B.; Johnston, A. K.; Wei, N.; Hedhili, M. N.; Wei, M.; Alsalloum, A. Y.; Maity, P.; Turedi, B.; Yang, C.; Baran, D.; Anthopoulos, T. D.; Han, Y.; Lu, Z.-H.; Mohammed, O. F.; Gao, F.; Sargent, E. H.; Bakr, O. M., Managing grains and interfaces via ligand anchoring enables 22.3%-efficiency inverted perovskite solar cells. *Nature Energy* **2020**.

22.   National Renewable Energy Laboratory. Best research-cell efficiencies. *https://www.nrel.gov/pv/assets/pdfs/best-research-cell-efficiencies.20200128.pdf*.

23.   Lin, K.; Xing, J.; Quan, L. N.; de Arquer, F. P. G.; Gong, X.; Lu, J.; Xie, L.; Zhao, W.; Zhang, D.; Yan, C.; Li, W.; Liu, X.; Lu, Y.; Kirman, J.; Sargent, E. H.; Xiong, Q.; Wei, Z., Perovskite light-emitting diodes with external quantum efficiency exceeding 20 per cent. *Nature* **2018,** *562* (7726), 245-248.

24.   Cao, Y.; Wang, N.; Tian, H.; Guo, J.; Wei, Y.; Chen, H.; Miao, Y.; Zou, W.; Pan, K.; He, Y.; Cao, H.; Ke, Y.; Xu, M.; Wang, Y.; Yang, M.; Du, K.; Fu, Z.; Kong, D.; Dai, D.; Jin, Y.; Li,

G.; Li, H.; Peng, Q.; Wang, J.; Huang, W., Perovskite light-emitting diodes based on spontaneously formed submicrometre-scale structures. *Nature* **2018,** *562* (7726), 249-253.

25.　　Park, M.-H.; Park, J.; Lee, J.; So, H. S.; Kim, H.; Jeong, S.-H.; Han, T.-H.; Wolf, C.; Lee, H.; Yoo, S.; Lee, T.-W., Efficient Perovskite Light-Emitting Diodes Using Polycrystalline Core–Shell-Mimicked Nanograins. *Advanced Functional Materials* **2019,** *29* (22), 1902017.

26.　　Zhao, B.; Bai, S.; Kim, V.; Lamboll, R.; Shivanna, R.; Auras, F.; Richter, J. M.; Yang, L.; Dai, L.; Alsari, M.; She, X.-J.; Liang, L.; Zhang, J.; Lilliu, S.; Gao, P.; Snaith, H. J.; Wang, J.; Greenham, N. C.; Friend, R. H.; Di, D., High-efficiency perovskite–polymer bulk heterostructure light-emitting diodes. *Nature Photonics* **2018,** *12* (12), 783-789.

27.　　Protesescu, L.; Yakunin, S.; Bodnarchuk, M. I.; Krieg, F.; Caputo, R.; Hendon, C. H.; Yang, R. X.; Walsh, A.; Kovalenko, M. V., Nanocrystals of Cesium Lead Halide Perovskites (CsPbX3, X = Cl, Br, and I): Novel Optoelectronic Materials Showing Bright Emission with Wide Color Gamut. *Nano Lett* **2015,** *15* (6), 3692-3696.

28.　　Swarnkar, A.; Marshall, A. R.; Sanehira, E. M.; Chernomordik, B. D.; Moore, D. T.; Christians, J. A.; Chakrabarti, T.; Luther, J. M., Quantum dot-induced phase stabilization of alpha-CsPbI3 perovskite for high-efficiency photovoltaics. *Science* **2016,** *354* (6308), 92-95.

29.　　Song, J. Z.; Li, J. H.; Li, X. M.; Xu, L. M.; Dong, Y. H.; Zeng, H. B., Quantum Dot Light-Emitting Diodes Based on Inorganic Perovskite Cesium Lead Halides (CsPbX3). *Adv Mater* **2015,** *27* (44), 7162-+.

30.　　Jellicoe, T. C.; Richter, J. M.; Glass, H. F. J.; Tabachnyk, M.; Brady, R.; Dutton, S. E.; Rao, A.; Friend, R. H.; Credgington, D.; Greenham, N. C.; Bohm, M. L., Synthesis and Optical Properties of Lead-Free Cesium Tin Halide Perovskite Nanocrystals. *J Am Chem Soc* **2016,** *138* (9), 2941-2944.

31.　　Zhang, D. D.; Eaton, S. W.; Yu, Y.; Dou, L. T.; Yang, P. D., Solution-Phase Synthesis of Cesium Lead Halide Perovskite Nanowires. *J Am Chem Soc* **2015,** *137* (29), 9230-9233.

32.　　Pan, A. Z.; He, B.; Fan, X. Y.; Liu, Z. K.; Urban, J. J.; Alivisatos, A. P.; He, L.; Liu, Y., Insight into the Ligand-Mediated Synthesis of Colloidal CsPbBr3 Perovskite Nanocrystals: The Role of Organic Acid, Base, and Cesium Precursors. *Acs Nano* **2016,** *10* (8), 7943-7954.

33.　　Shamsi, J.; Dang, Z. Y.; Bianchini, P.; Canale, C.; Di Stasio, F.; Brescia, R.; Prato, M.; Manna, L., Colloidal Synthesis of Quantum Confined Single Crystal CsPbBr3 Nanosheets with Lateral Size Control up to the Micrometer Range. *J Am Chem Soc* **2016,** *138* (23), 7240-7243.

34.　　Imran, M.; Di Stasio, F.; Dang, Z. Y.; Canale, C.; Khan, A. H.; Shamsi, J.; Brescia, R.; Prato, M.; Manna, L., Colloidal Synthesis of Strongly Fluorescent CsPbBr3 Nanowires with Width Tunable down to the Quantum Confinement Regime. *Chem Mater* **2016,** *28* (18), 6450-6454.

35.　　Bekenstein, Y.; Koscher, B. A.; Eaton, S. W.; Yang, P. D.; Alivisatos, A. P., Highly Luminescent Colloidal Nanoplates of Perovskite Cesium Lead Halide and Their Oriented Assemblies. *J Am Chem Soc* **2015,** *137* (51), 16008-16011.

36.　　Manzi, A.; Tong, Y.; Feucht, J.; Yao, E.-P.; Polavarapu, L.; Urban, A. S.; Feldmann, J., Resonantly enhanced multiple exciton generation through below-band-gap multi-photon absorption in perovskite nanocrystals. *Nature Communications* **2018,** *9* (1), 1518.

37.　　Li, X. M.; Wu, Y.; Zhang, S. L.; Cai, B.; Gu, Y.; Song, J. Z.; Zeng, H. B., CsPbX3 Quantum Dots for Lighting and Displays: Room-Temperature Synthesis, Photoluminescence Superiorities, Underlying Origins and White Light-Emitting Diodes. *Adv Funct Mater* **2016,** *26* (15), 2435-2445.

38.   Sun, S. B.; Yuan, D.; Xu, Y.; Wang, A. F.; Deng, Z. T., Ligand-Mediated Synthesis of Shape-Controlled Cesium Lead Halide Perovskite Nanocrystals via Reprecipitation Process at Room Temperature. *Acs Nano* **2016,** *10* (3), 3648-3657.

39.   Wei, S.; Yang, Y. C.; Kang, X. J.; Wang, L.; Huang, L. J.; Pan, D. C., Room-temperature and gram-scale synthesis of CsPbX3 (X = Cl, Br, I) perovskite nanocrystals with 50-85% photoluminescence quantum yields. *Chem Commun* **2016,** *52* (45), 7265-7268.

40.   Akkerman, Q. A.; Gandini, M.; Di Stasio, F.; Rastogi, P.; Palazon, F.; Bertoni, G.; Ball, J. M.; Prato, M.; Petrozza, A.; Manna, L., Strongly emissive perovskite nanocrystal inks for high-voltage solar cells. *Nat Energy* **2017,** *2* (2).

41.   Jurow, M. J.; Lampe, T.; Penzo, E.; Kang, J.; Koc, M. A.; Zechel, T.; Nett, Z.; Brady, M.; Wang, L.-W.; Alivisatos, A. P.; Cabrini, S.; Brütting, W.; Liu, Y., Tunable Anisotropic Photon Emission from Self-Organized CsPbBr3 Perovskite Nanocrystals. *Nano Letters* **2017,** *17* (7), 4534-4540.

42.   Xu, Y. Q.; Chen, Q.; Zhang, C. F.; Wang, R.; Wu, H.; Zhang, X. Y.; Xing, G. C.; Yu, W. W.; Wang, X. Y.; Zhang, Y.; Xiao, M., Two-Photon-Pumped Perovskite Semiconductor Nanocrystal Lasers. *J Am Chem Soc* **2016,** *138* (11), 3761-3768.

43.   Loiudice, A.; Saris, S.; Oveisi, E.; Alexander, D. T. L.; Buonsanti, R., CsPbBr3 QD/AlOx Inorganic Nanocomposites with Exceptional Stability in Water, Light, and Heat. *Angew Chem Int Edit* **2017,** *56* (36), 10696-10701.

44.   Moroz, P.; Kholmicheva, N.; Razgoniaeva, N.; Burchfield, D.; Sharma, N.; Acharya, A.; Zamkov, M., Optical techniques for probing the excited state dynamics of quantum dot solids. *Chem Phys* **2016,** *471*, 59-68.

45.   Kagan, C. R.; Murray, C. B.; Nirmal, M.; Bawendi, M. G., Electronic Energy Transfer in CdSe Quantum Dot Solids. *Physical Review Letters* **1996,** *76* (9), 1517-1520.

46.   Crooker, S. A.; Hollingsworth, J. A.; Tretiak, S.; Klimov, V. I., Spectrally resolved dynamics of energy transfer in quantum-dot assemblies: Towards engineered energy flows in artificial materials. *Phys Rev Lett* **2002,** *89* (18).

47.   Kennedy, C. L.; Hill, A. H.; Massaro, E. S.; Grumstrup, E. M., Ultrafast Excited-State Transport and Decay Dynamics in Cesium Lead Mixed Halide Perovskites. *Acs Energy Lett* **2017,** *2* (7), 1501-1506.

48.   Guo, Z.; Manser, J. S.; Wan, Y.; Kamat, P. V.; Huang, L. B., Spatial and temporal imaging of long-range charge transport in perovskite thin films by ultrafast microscopy. *Nature Communications* **2015,** *6*.

49.   Yoon, S. J.; Guo, Z.; Dos Santos Claro, P. C.; Shevchenko, E. V.; Huang, L., Direct Imaging of Long-Range Exciton Transport in Quantum Dot Superlattices by Ultrafast Microscopy. *Acs Nano* **2016,** *10* (7), 7208-15.

50.   Saris, S.; Loiudice, A.; Mensi, M.; Buonsanti, R., Exploring Energy Transfer in a Metal/Perovskite Nanocrystal Antenna to Drive Photocatalysis. *The Journal of Physical Chemistry Letters* **2019,** *10* (24), 7797-7803.